

Ionoluminescence of Al, Cu, and Mo: Optical properties of aluminum*

M. Zivitz and E. W. Thomas

School of Physics, Georgia Institute of Technology, Atlanta, Georgia 30332

(Received 21 July 1975)

Impact of 10- to 30-keV H^+ and He^+ ions on polycrystalline Al, Cu, and Mo targets induces broad-band light emissions in the photon energy range of 2–6 eV; these emissions emanate from the target. For aluminum the emission is particularly intense, increases linearly with incident beam current, and is invariant in relative shape with projectile energy and angle of incidence. The dominant peak is at a photon energy of 2.4 eV; and a weak shoulder is observed at 3.3 eV. An electron-hole recombination model is shown to account for the general form of the emission band. We also calculate the electron density of states and the complex part of the dielectric constant ϵ_2 ; the energy-band structure based on Ashcroft's Al pseudopotential is presented in tabular form.

I. INTRODUCTION

Fast-ion impact on solid surfaces results in several types of radiant emission in the visible and near-uv region of the electromagnetic spectrum.^{1,2} Doppler-shifted atomic line emissions emanate from backscattered excited projectile atoms or ejected target atoms.³⁻⁵ Characteristic band emissions result from excited electrons within insulators and semiconductors; broad-band light emission has also been observed due to ion impact on metals.^{3,6} Here we report quantitative measurements of luminescence induced by 10- to 30-keV H^+ and He^+ impact on a variety of metals. Spectra took the form of bands (~1000- to 2000-Å full widths) observed in the photon energy range 2–6 eV. These bands were readily distinguished from atomic line emissions. For Al we observed emissions characteristic of the electrons within the solid. Several mechanisms have been previously suggested as sources of this or similar emission.^{3,7,8} In this paper, we consider several of these models further.

In Secs. II and III we present our experimental results and a discussion of these spectra. Section IV contains a few of the mechanisms we considered and the reasons for discarding them. These models were bremsstrahlung, transition radiation, and recombination radiation due to the decay of surface plasmons. This is followed in Sec. V by a theoretical treatment based on direct interband transitions for the emission in Al, which is shown to account for the observed spectrum.

Two calculations are made, to account for the source of the Al band. One prediction is based on a generalization of a model proposed by Mooradian in a study of photoluminescence of noble metals.⁷ This model is essentially electron-hole recombination by means of direct interband transitions between an occupied state (below the Fermi level)

and a vacancy (created below) by ion impact. We take the cavalier view of neglecting the thermalization of the carrier distribution which exists in excess of the equilibrium distribution. The second model is similar to the established picture of luminescence in insulators and semiconductors.⁹ The calculations use Ashcroft's empirical pseudopotential.¹⁰ We present analytic solutions for the roots of the four-band secular determinant at several symmetry points of the Brillouin zone. These solutions are of interest as they provide energy gaps which differ slightly from the commonly quoted two-band gap result $E_g = 2V_G$.

As a check on our numerical procedures, we compute the electron density of states and compare the resultant Fermi level with Ashcroft's result (Ashcroft obtained his Fermi level in a quite different manner). We compute the complex part of the dielectric constant ϵ_2 , as a check on our matrix elements. Fair agreement is obtained at 0.5 eV and excellent agreement is obtained at 1.5 eV with the nine-band model of Brust.¹¹

Section VI contains a brief comparison between experiment and theory. The Appendix contains the band structure of Al on a mesh convenient for tabulation.

II. EXPERIMENTAL RESULTS AND DISCUSSION

The apparatus used in these luminescence experiments has been previously described.⁵ Ions from an rf discharge source were momentum analyzed, collimated, and directed onto polycrystalline target surfaces at some angle ϕ with respect to the target-surface normal. Emissions from these targets were viewed at 90° to the incident beam by a grating monochromator, followed by a photomultiplier tube provided with photon-counting instrumentation. Projectiles of H^+ , H^0 , and He^+ at 5- to 30-keV impact energy provided ~1- μ A

beams of 2-mm diameter at the target surface. Projectile beam currents were monitored on a Faraday cup that could be periodically inserted into the beam line. Figure 1 gives a schematic view of the beam-target-monochromator geometry. Ambient pressures were maintained at 10^{-9} Torr in the target chamber using an ion pump. Targets were mechanically polished with 0.5- μm alumina and electropolished. Materials Research Corp. provided these metals with a purity of 99.97%.

The detection efficiency of the monochromator has been calibrated using a tungsten filament lamp as a standard of emission intensity. A lamp calibrated by the Eppley Laboratories according to the method of the National Bureau of Standards¹² was used as the primary standard for the visible spectrum. A Phillips tungsten filament lamp was used as the secondary standard because of its more convenient size. To extend the calibration to include ultraviolet wavelengths (3000–4000 Å), the branching ratio method was employed.^{13,14} Nitrogen gas was introduced into the target chamber and excited by a 25-keV beam of H^+ or He^+ ions. Observations were made of the relative signals from the second positive system of N_2 and the first negative system of N_2^+ . Theoretical predictions of the relative intensities in these two spectral systems were obtained from the work of Thomas *et al.*¹⁵ and Burns *et al.*¹⁶ Hence, the relative sensitivity was established and could be normalized to the absolute sensitivity measured at visible wavelengths using the standard lamp. The monochromator detects only emissions perpendicular to the ion-beam direction. In estimating the number of photons produced per incident ion we have assumed that the emission is isotropic. The detection efficiency of the monochromator-detector system was calibrated to within $\pm 50\%$.

For 25-keV H^+ impact energy, the observed spectra for Al, Mo, and Cu targets are given in

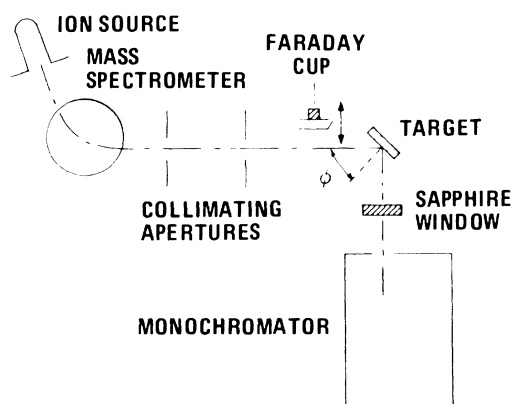


FIG. 1. Schematic diagram of the apparatus.

Fig. 2. These spectra have been corrected for the transmission function of the monochromator-detector system and are on an absolute scale. With the exception of Al, we arbitrarily designate the band at 3250 Å, "band I" and the band at 4200 Å, "band II." Band I for Cu has been previously reported.³ Our raw spectral data indicate that band I peaks at about 3250 Å, and the intensity drops sharply to 3000 Å. Unfortunately, it was impossible to perform precise calibrations of detection sensitivity at wavelengths below 3250 Å, and we have therefore omitted the lower-wavelength data from Fig. 2. Similar spectra were observed for He^+ ions incident on these same metals although band II was considerably reduced in such cases.

Spectra observed with targets of W, and Nb were similar to those of Cu and Mo in that band I was always present and very intense; band II was observed only with Cu, Mo, and W. Approximate estimates of emission intensity of these bands are given in Table I. The principal purpose of the table is to indicate that the aluminum emission is by far the most intense and is located primarily in the visible region; by contrast all other targets give essentially similar emission spectra with a peak at around 3250 Å.

It has been suggested² that the broadband emission observed under ion bombardment might be due to fluorescence of the window through which the target is observed; such fluorescence might be caused by secondary electrons, or reflected projectiles from the target, being incident on the window. Thus suggestion was tested by setting the optical system to view the window but not the target inside the vacuum system. With this configuration no emissions were observed; this test shows

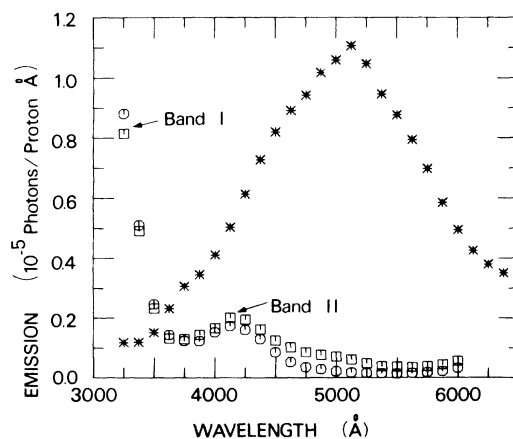


FIG. 2. Luminescence of Al, Mo, and Cu induced by 25-keV H^+ impact at an incidence angle ϕ of 45° . Stars, Al data; squares, Mo data ($\times 25$); circles, Cu data ($\times 20$).

conclusively that window fluorescence was not the origin of the emission. Other tests included biasing the target to suppress secondary ions and electrons; this causes no change to the observed spectra. To ensure that targets were free of contamination they were subject to bombardment by argon or neon ion beams for extended time periods to permit sputter cleaning. The form of the broadband emissions was unaffected by this treatment.

In the case of aluminum and copper, targets we made tests to ensure that the broadband emissions emanated from the target surface and not from some range in front of these surfaces. The optical system (see Fig. 1) was provided with a series of baffles so that the field of view at the target was restricted to a width of 2 mm in the plane of the ion beam. The target was set at an angle ϕ of 45° and irradiated with a beam collimated to 2-mm diameter. Then the target was translated along the beam path for a distance of 7 mm to either side of the intersection of the monochromator axis with the ion-beam axis; the spectrum was monitored as a function of the target position. At a target displacement of ± 2 mm from the intersection of the ion beam and optical axis, the intensity of all spectral components was negligible. This indicates that the source of emission occupied a region of 2 mm extent in the plane containing the ion-beam axis; this is exactly the region irradiated by the ion beam. As a further test the angle of beam incidence ϕ was set at zero degrees and the optical system, with the 2-mm field of view, was arranged to view a region centered at 1 mm in front of the surface; no optical signals were observed. Allowing for statistical variations in signals and mechanical errors in defining position, we consider the accuracy of the location of the

source of emission to be about 0.5 mm. Thus, our observations show that the source of emission lies at the surface, or certainly no more than 0.5 mm in front of the surface. Because of the necessity of using mechanical systems for this test it is not feasible to appreciably improve the spatial resolution. We conclude that there is no evidence that the source of continuum emission does not lie in the surface.

From the above tests of spatial distributions one can also derive some information on the velocity distribution of sputtered atoms. With He^+ impact on Al we can also observe emission from sputtered aluminum atoms in the multiplets at 3089 and 3956 Å. These exhibit the same spatial distribution as the continuum emission. Utilizing the known lifetimes of these excited aluminum states¹⁷ we estimate the average velocity of the sputtered aluminum atoms to be less than 5×10^6 cm sec⁻¹. There have been no measurements of sputtered aluminum velocity distributions. However, if one uses the simple theoretical estimate of average sputtered particle energy given by Dearnaley *et al.*,¹⁸ and a cohesive energy for aluminum¹⁹ of 3.34 eV/atom one gets an average velocity of 10^6 cm/sec; this is consistent with our observations.

There have been various previous studies of luminescence in metals where broadband light emission has been observed. Van der Weg and Lugujo⁶ observed emission induced by 40-keV Ar^+ -ion impact on various metals; they found broad bands only when the *d* bands of the metals were half-filled (notable Mo). Mooradian⁷ reported a photoluminescence in Cu with peak emission at 2 eV. Our spectra do not correlate with any of these previous observations. Bonnot *et al.*⁸ report spectra induced by 25-keV electron impact on cop-

TABLE I. Observed emissions and relative transition rates at band maxima, for 25-keV H^+ and He^+ impact on various metals at 60° angle of incidence. For each projectile the rates are normalized to 100 arbitrary units; a blank denotes negligible emission. No correction for spectral transmission function of system has been used here.

Projectile	Target	Band I		Band II	
		Location (Å)	Strength (relative)	Location (Å)	Strength (relative)
H^+	Al			5200	100
	Cu	3250	6.8	4200	1.1
	Nb	3300	2.4		
	Mo	3300	3.7	4250	1.1
	W	3250	16	4000	3.1
He^+	Al			5200	100
	Cu	3250	0.8		
	Nb	3250	0.8		
	Mo	3500	3.0		
	W	3250	6.0		

per that show some similarities with our spectra, particularly in the strong emission of band I around 3250 Å; there are considerable differences in detail.

The similarity of the emissions observed from Cu, Nb, Mo, and W targets suggests that the excitation mechanism is the same in all these cases and is probably not closely related to the detailed band structure of the solid. By contrast aluminum has a far more intense emission, different from the other metals studied. We shall offer no explanation of the emission from the noble and transition metals and, with few exceptions, proceed to discuss only the rather intense characteristic emission of aluminum.

III. CHARACTERISTICS OF EMISSION FROM ALUMINUM

The impact of a 25-keV He⁺ beam on an aluminum surface gave a spectrum consisting primarily of the broad band shown in Fig. 2 but including also weak atomic lines of aluminum around 3089 and 3956 Å; for H⁺ impact the spectrum was the same except that the aluminum atomic lines were absent.

There was concern that the emission might be related to oxide layers on the surface and the following tests were made. For a new target bombarded with He⁺ for the first time the intensity of aluminum lines from sputtered atoms decreased by a factor of 4 over an extended period of time. Bombardment with Ar⁺ caused a similar but more rapid transient. Admitting oxygen at a pressure of 10⁻⁴ Torr to the target region caused the intensity of the atomic lines to increase back to approximately the same level as observed with a new target. A similar behavior has been observed elsewhere²⁰ during bombardment of Al by Ne⁺ and is interpreted as being due to oxide formation.²⁰ We adopt that same explanation here. Following Kelly and Kerkdijk²⁰ we believe that the constant intensity observed after prolonged bombardment indicates the removal of oxide and the formation of a clean atomic surface; exposure to O₂ causes reformation of an oxide layer. After the clean surface condition was obtained the signal remained constant indefinitely. Upon removing the beam for many hours and then recommencing bombardment there was again a short-term decay indicating some recontamination of the surface. For all detailed measurements presented here the surface was prebombarded with Ar⁺ to attain what we believe is an oxide-free surface. Some transient effects were also observed in the intensity of the continuum spectrum. During initial bombardment of a new spot with He⁺ ions the intensity of con-

tinuum emission decreased by a factor of two. By contrast with sputtered atomic lines the intensity did not change on exposing the target to a pressure of 10⁻⁴ Torr of O₂, or removal of the beam for extended periods. Exposure of O₂ is known²⁰ to cause reformation of the oxide and we observe no change to the continuum; we therefore conclude that the continuum emission is not linked to oxide formation. The origin of the initial transient in continuum emission is not clear. We note, however, that bombardment of aluminum by a 30-μA/cm² He⁺ beam causes considerable damage to the surface that is clearly visible under a microscope. We suggest that the intensity of continuum emission is effected by this damage. In the following sections we shall postulate that emission is due to a radiative electron-hole recombination mechanism. Defect sites will certainly induce quenching of such luminescence by nonradiative recombination mechanisms as has been frequently observed in luminescence of alkali halides.²¹ Our conclusion from these observations is that the surfaces were free of oxide contamination and that the luminescence of aluminum may be quenched by damage to the target.

As a further test for contaminants we examined the spectrum induced by Ar⁺ on Al. The spectrum consisted only of aluminum lines and there was no evidence of CH bands that have been observed by others²² and which indicates hydrocarbon contamination. Also there was no "blackening" of the surface; such blackening was seen by Kelly and Kerkdijk²⁰ when bombarding Al with low-beam currents of Ne⁺ in a poor (10⁻⁶-Torr) vacuum and was interpreted by them as carbon build up from impurity hydrocarbons.

We tested the dependence of the broadband emission on the incident-ion current. The current was in fact altered by deflecting the beam by a square wave signal fed to a pair of condenser plates. The chopping frequency was 10 kHz and the duty cycle was altered to vary the beam current. The broadband spectral shape was independent of the beam current and the intensity increased linearly with current up to the maximum current density available (30 μA/cm²).

Studies were made of the broadband shape as a function of projectile energy (10–30 keV) and projectile incidence angle on the surface ($\phi = 5^\circ$ – 70°). No systematic changes to the spectral shape were observed.

Measurements were made of the intensity of the band emission as a function of the angle ϕ between the projectile beam and surface normal. Before starting detailed measurements the target was turned to the largest incidence angle ($\phi = 75^\circ$) and the beam directed on the surface for an extended

time period until the signal was constant; this ensured that any transient effects due to sputter cleaning of the target were complete. Then the intensity was monitored as a function of incidence angle. Since we had already shown the shape of the spectrum to be independent of incidence angle it was satisfactory to monitor intensity only at a single wavelength. Figure 3 shows the measured intensity as a function of the tangent of the incidence angle. At the energy of which the data are taken (25 keV), the range of protons in aluminum is of the order²³ 2000 Å; if the excitation events occur throughout the projectiles range then the emission should occur throughout the 2000-Å path. However, the absorption coefficient α for visible light in aluminum is of the order 10^6 cm^{-1} ; thus in practice the observer will detect only the emissions occurring within approximately 100 Å of the surface. The observed emission must therefore be confined to a relatively shallow region close to the surface. It can be shown quite easily that with the sources of emission localized close to the surface in a depth of the order α^{-1} , the observed intensity should vary as the tangent of the incidence angle ϕ . Kerkdijk and Thomas³ showed that the 3250-Å band induced by He⁺ on copper (band I of Fig. 2) did in fact vary in this manner. In Fig. 3 we show a line indicating a least squares fit of the data to a tangent function. Clearly the data does not follow a simple tangent function. The discrepancy may not be of great significance since our model is very simplistic and neglects such factors as internal reflection of light at the surface, nonuniform

distribution of emitting sources, and influence of radiation damage on the optical properties of the solid. Moreover, we can use our previous backscattering computations³ to show that at large incidence angles a substantial fraction of the projectiles are backscattered out of the surface; for an angle ϕ of 75° as much as 20% of the incident 25-keV proton flux will in fact backscatter out of the surface. Thus the disagreement, indicated in Fig. 3 between experiment and the simplistic model, is not at all surprising.

The total intensity in the aluminum band was determined using the absolute calibration of sensitivity and integrating the emission spectrum between 3250 and 6500 Å. The emission from the surface was assumed to be isotropic. For 25-keV H⁺ on the aluminum target we determine an emission into all directions of 0.02 ± 0.01 photons per incident ion. The limit of error specified represents the absolute reproducibility of our data. An estimate of the relative reproducibility of our data is $\pm 5\%$. A 25-keV ion will lose some kiloelectronvolts of energy in the approximately 100-Å depth from which radiation can escape. Thus, only a small fraction of the energy deposited in the solid is in fact used in the formation of excited states.

We did attempt to observe polarization of the emission using a simple polaroid analyzer. Certain of the mechanisms we shall examine as possible sources of the emission are expected to exhibit strong polarization with respect to the direction of the projectile beam. No significant polarization was observed for any angle of projectile incidence on the surface.

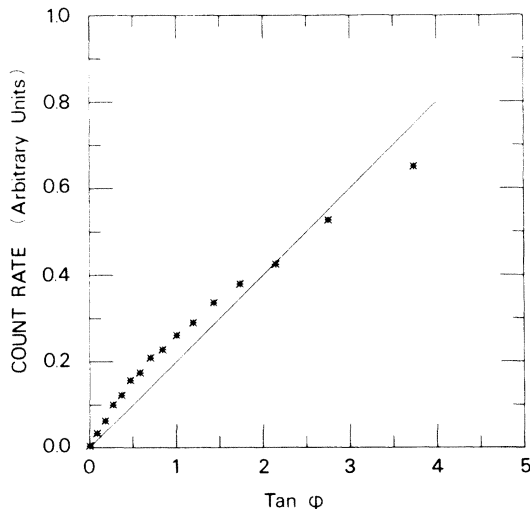


FIG. 3. Al emission, induced by 25-keV H⁺ impact, at fixed wavelength 4750 Å, as a function of the tangent of the incidence angle ϕ . Stars, experimental data points; straight line, a least-squares fit of a tangent function to the data.

IV. POSSIBLE EMISSION MECHANISMS

The various tests detailed previously confirm that the broad band emission is not an artifact of the experimental arrangement. The emission has its origin in the target surface and is excited by the incident projectile. This conclusion holds for all the metal targets studied. Various possible mechanisms were considered as the source of the broadband emission, and we discuss here those that were not consistent with our observations.

Boersch *et al.*²⁴ have considered the possibility that broadband light emission induced by electron impact on solids is due to bremsstrahlung or transition radiation. Goldsmith and Jelley²⁵ have in fact observed transition radiation as protons with MeV energies collide with metal targets. These two mechanisms are well understood, and Boersch *et al.* give equations from which the intensity of emission can be computed. Using these formulations for the case of 25-keV H⁺ incident on a metal target at 45° to the surface normal, we predict

that the emission due to either bremsstrahlung or to transition radiation should be of the order 10^{-12} photons per incident proton emitted in a wavelength interval of 1 Å into a solid angle of one steradian. This is some seven orders of magnitude smaller than the intensities we observe. Moreover, both bremsstrahlung and transition radiation should be strongly polarized whereas our observed emissions are not polarized.

We conclude that neither of these mechanisms provides a significant contribution to our observed emission.

High-energy electron impact on metals produces broadband emission structure that has been identified as a decay of the surface plasmon. Boersch *et al.*²⁴ claim that electron impact on silver yields the radiative decay of surface plasmons. For the case of unoxidized aluminum the surface plasmon has an energy of 10.3 eV. For an oxidized surface, this energy is lowered to 7 eV (1770 Å). On the basis of the location of the Al band emission (4750 Å), the surface plasmon model was discarded. Also in the case of the other metals studied here (Cu, Mo, W, and Nb) the surface plasmon energy does not correspond to the position of the principal emission peak (3250 Å).

On the basis of the above arguments it is considered that the emissions observed here are not attributable to bremsstrahlung, transition radiation, nor to decay of plasmons.

The emission from the aluminum target has a rather different spectral distribution from that of the other metals considered; moreover it is at least one order of magnitude more intense. We propose that the emission from aluminum is due to an electron-hole recombination mechanism; the initial excitation being provided by the interaction of the projectile with valence electrons. Bonnot *et al.*⁸ have previously invoked a recombination mechanism to explain cathodoluminescence in copper, although they make no attempt to predict the spectrum in detail. In Sec. V we discuss certain of the optical properties of aluminum and develop an approximate prediction of the spectrum expected from electron hole recombination. We offer no further attempts to explain the emissions from Cu, Mo, W, and Nb targets.

V. OPTICAL PROPERTIES OF ALUMINUM

A. Definition of terms

The objective here is to consider two models for the band emission of Al. Detailed agreement with experiment is not sought. The Fermi distribution function is not handled self-consistently, and details of the excitation process are not considered. The distribution function $\mathcal{F}(\vec{k})$, with \vec{k} a wave vector

in reciprocal space, is somehow different from the equilibrium distribution since carriers (electrons and holes) are generated continuously by collisions of the projectile with the target; this is a non-thermal process.²⁶ Self-consistency (fixed concentration of electrons) can be obtained by the introduction of a quasi-Fermi level; in our calculations we do not impose this self-consistency, since we mainly seek only quantitative agreement with the energy location of structure. The following definitions are introduced, to facilitate discussion of the models. Direct (vertical) interband transitions involve initial and final states which lie at the same point (wave vector \vec{k}) in the first Brillouin zone (reduced zone scheme).^{27,28} If $E_i(\vec{k})$ and $E_f(\vec{k})$ are the energies of the initial band i and final band f , respectively, then in optical absorption at photon energy $E = \hbar\omega$ the locus of all points which satisfy

$$E_f(\vec{k}) - E_i(\vec{k}) = E \quad (1)$$

defines a surface of constant interband energy difference (the optical band). The joint density of states (JDOS) per unit volume is defined by

$$J(E) = \frac{2}{(2\pi)^3} \sum_{i,f} \int'_{BZ} d^3k \delta[E_f(\vec{k}) - E_i(\vec{k}) - E], \quad (2)$$

where the prime denotes that the integration is to be performed only over regions of \vec{k} space in which $E_f > E_F \geq E_i$, where E_F is the Fermi energy (BZ denotes Brillouin zone). Since the summation is performed over all band pairs, the JDOS represents the total number of direct transitions which can contribute to the optical absorption at photon energy E . The properties of the energy conserving Dirac delta function allow the reduction of Eq. (2) to the familiar surface integral

$$J(E) = \frac{2}{(2\pi)^3} \sum_{i,f} \int'_{BZ} dS_{\vec{k}} / |\nabla_{\vec{k}}(E_f - E_i)|, \quad (3)$$

the integration being done over the sets of surfaces defined by Eq. (1).

In a similar way, we define quantities for optical emission due to electron-hole recombination. The absolute meaning of the similar quantities is that we are neglecting the thermalization (rising of holes and falling of electrons due to phonon emission) of the excess carrier distribution generated by ion impact. We assume this to be a small frozen distribution in excess of the equilibrium distribution and that the Fermi level is unperturbed. We have by definition at wave vector \vec{k}

$$E_i(\vec{k}) - E_f(\vec{k}) = E, \quad (4)$$

where $E = \hbar\omega$ is the emission photon energy. Again, $E_i(\vec{k})$ is the initial band energy and $E_f(\vec{k})$ is the final band energy. Here the upper band state \vec{k}_i is

occupied, the lower-band state \vec{k}_f is unoccupied:

$$J(E) = \frac{2}{(2\pi)^3} \sum_{i,f} \int_{\text{BZ}} d^3k \delta[E_i(\vec{k}) - E_f(\vec{k}) - E]. \quad (5)$$

The disposition of the initial and final band energies relative to the Fermi level will be designated when we discuss particular models. Again, this reduces to a surface integral

$$J(E) = \frac{2}{(2\pi)^3} \sum_{i,f} \int_{\text{BZ}} dS_{\vec{k}} / |\nabla_{\vec{k}}(E_i - E_f)|, \quad (6)$$

the integration being carried out over the sets of surfaces defined by Eq. (4).

The JDOS for absorption suffices to account for much of the structure in the complex part of the dielectric constant ϵ_2 in semiconductors.²⁹ However, much of the oscillator strength of Al is exhausted by structure-poor interband absorption so that it becomes necessary to include the relevant matrix elements to provide a truly satisfactory explanation of the interband absorption. However, one can sometimes anticipate the photon-energy location of structure in simple metals, using Harrison's parallel-band model.³⁰

In what follows we shall first discuss the calculation of energy band structure and wave functions for aluminum. We shall then test the adequacy of the computed band structure by calculating the conventional electron density of states which may be compared with previous predictions. In pre-

dicting the recombination rate one must also include the relevant matrix elements; to ensure the adequacy of the values used, we have also calculated the complex part of the dielectric constant ϵ_2 ; again this is compared with previous calculations. Finally, we utilize a development of Eq. (6) including the relevant matrix elements to predict a spontaneous recombination rate.

B. Band structure of aluminum

To generate the energy band structure and wave functions an empirical pseudopotential model with four orthogonalized plane waves was employed.²⁷ Ashcroft's¹⁰ local pseudopotential coefficients $V_{\vec{G}}$, defined via

$$V_P(\vec{r}) = \sum_{\vec{G}} V_{\vec{G}} e^{i\vec{G}\cdot\vec{r}} \approx V_{111} e^{i\vec{G}_{111}\cdot\vec{r}} + V_{11\bar{1}} e^{i\vec{G}_{11\bar{1}}\cdot\vec{r}} + V_{200} e^{i\vec{G}_{200}\cdot\vec{r}}, \quad (7)$$

where $V_{11\bar{1}} = V_{111} = 0.2435$ eV and $V_{200} = 0.7646$ eV were used together with the free electron mass and the lattice constant³¹ $a = 4.04145$ Å. Reciprocal-lattice vectors \vec{G} are in units of $2\pi/a = 1$; e.g. $\{(2\pi/a), (2\pi/a), (2\pi/a)\}$ is written $(1, 1, 1)$. We worked within Ashcroft's¹⁰ choice of the $\frac{1}{48}$ th symmetry sector of the Brillouin zone. In units of $\hbar^2/2m = 1$ and $2\pi/a = 1$, the secular determinant for the one-electron pseudo-wave-equation, formally, took a simple form

$$\begin{vmatrix} \vec{k}^2 - E_{\vec{k}} & V_{111} & V_{111} & V_{200} \\ V_{111} & [\vec{k} - (1, 1, 1)]^2 - E_{\vec{k}} & V_{200} & V_{111} \\ V_{111} & V_{200} & [\vec{k} - (1, 1, \bar{1})]^2 - E_{\vec{k}} & V_{111} \\ V_{200} & V_{111} & V_{111} & [\vec{k} - (2, 0, 0)]^2 - E_{\vec{k}} \end{vmatrix} = 0, \quad (8)$$

when the pseudo-wave-function was expanded

$$\phi_{\vec{k}}(\vec{r}) = a_{\vec{k}} e^{i\vec{k}\cdot\vec{r}} + a_{\vec{k}-(1,1,1)} e^{i[\vec{k}-(1,1,1)]\cdot\vec{r}} + a_{\vec{k}-(1,1,\bar{1})} e^{i[\vec{k}-(1,1,\bar{1})]\cdot\vec{r}} + a_{\vec{k}-(2,0,0)} e^{i[\vec{k}-(2,0,0)]\cdot\vec{r}}. \quad (9)$$

Now through the definitions

$$\begin{aligned} T_1 &= \vec{k}^2 - E_{\vec{k}}, \\ T_2 &= [\vec{k} - (1, 1, 1)]^2 - E_{\vec{k}}, \\ T_3 &= [\vec{k} - (1, 1, \bar{1})]^2 - E_{\vec{k}}, \\ T_4 &= [\vec{k} - (2, 0, 0)]^2 - E_{\vec{k}} \end{aligned} \quad (10)$$

the secular determinant was expanded and cast into the form

$$(T_1 T_4 - V_{200}^2)(T_2 T_3 - V_{200}^2) - V_{111}^2 \times (T_1 + T_4 - 2V_{200})(T_2 + T_3 - 2V_{200}) = 0. \quad (11)$$

At the choice of symmetry points given in Table II, two or more kinetic-energy terms T_i of Eq. (11) became equal. Some or all of the roots were then found by factoring. The results for the W point were conventional. We believe the results for the other symmetry points are somewhat original. Obviously the energy gaps differ somewhat from the standard two-band predictions (e.g. at the L point: $E_{12} = E_{34} = 2V_{111}$ and at the X point: $E_{12} = E_{34} = 2V_{200}$ in the two-band model). We hope these analytical results for this popular four-band model prove useful to future workers who seek checks on their numerical procedures.

The transformation which diagonalized the Hamiltonian matrix to produce the eigenvalues also defined the pseudo wave functions. These were subsequently used to evaluate the matrix elements to be introduced below. Division of the ΓX line into 184 equal segments defined the linear step size which divided the entire volume of the $\frac{1}{48}$ th symmetry sector into a cubic mesh of 538 385 points. When careful use was made of the number of like vectors, we obtained the equivalent of four-band energies at exactly 24 612 968 points throughout the Brillouin zone.

The energy band structure for a number of symmetry lines and other lines are presented as an appendix in both graphical and tabular form. The new zero of energy was chosen to be the bottom of the first band, and the Fermi level was given by Ashcroft.¹⁰ We number band indices 1–4 in order of increasing energy for a given wave vector \vec{k} ; in this way, bands do not cross. These bands given in the Appendix provide a somewhat more extensive presentation of energy levels than preceding work such as that by Ashcroft¹⁰; however, the present results are in complete agreement with the preceding work wherever comparison is possible.

C. Numerical procedures and density of states

To provide a check on the accuracy of the band structure, we generated in a conventional manner the electron density of states (DOS) per unit volume using the form [see Eqs. (2)–(6)]

$$D(E) = \frac{2}{(2\pi)^3} \sum_j \int_{\text{BZ}} d^3k \delta[E_j(\vec{k}) - E]. \quad (12)$$

In calculations of any of these density functions (and similar integrals below) it is simplest to work directly with the volume integrals which contain the Dirac delta energy conserver. With judicious interpretation, the Dirac delta became a Kronecker delta. We rewrote Eq. (12) as

$$D(E_m) = \frac{2}{(2\pi)^3} \frac{(\Delta k)^3}{\Delta E} \sum_{\vec{k}} L V_{\vec{k}} \times \sum_{j=1}^4 \Delta \left(E_m - \frac{\Delta E}{2}, E_j(\vec{k}), E_m + \frac{\Delta E}{2} \right) \quad (13)$$

with

$$\Delta \left(E_m - \frac{\Delta E}{2}, E_j, E_m + \frac{\Delta E}{2} \right) = \begin{cases} 0, & |E_j - E_m| > \frac{\Delta E}{2}, \\ 1, & |E_j - E_m| \leq \frac{\Delta E}{2}. \end{cases}$$

The number of vectors equivalent to those within the symmetry sector were incorporated in the “like vector” $L V_{\vec{k}}$ term.³² The sum over \vec{k} was restricted to this sector. In the generation of the band structure, each of the 538 385 \vec{k} vectors, the number of like vectors, the four eigenvalues, and the four wave functions were calculated and stored on magnetic tape. We then evaluated the contribution to the DOS at a given electron “bin” energy E_m of width $\Delta E = 0.1$ eV. Histograms were gen-

TABLE II. Exact eigenvalues^a of 4-band secular determinant for fcc crystals at various symmetry points. Vertical interband gap energies are likewise exactly given by $E_g = E_i(\vec{k}) - E_j(\vec{k})$. Note that the E values are the empty lattice ($V_C = 0$) eigenvalues ($E = \hbar^2 \vec{k}^2 / 2m$) at the respective points; a blank or approximate entry corresponds to an irreducible cubic polynomial. For simplifying the display of this table we have written V_1 for V_{111} and V_2 for V_{200} ; the symbols A , B , and C are defined as follows:

$$A = \frac{1}{2} \left[\left(\frac{8}{3} E_L \right)^2 + 4(V_2 - V_1)^2 \right]^{1/2},$$

$$B = \frac{1}{2} \left[\left(\frac{8}{3} E_L \right)^2 + 4(V_2 + V_1)^2 \right]^{1/2},$$

$$C = \frac{1}{2} \left[E_X^2 + (4V_1)^2 \right]^{1/2}.$$

BSW symbol ^b	\vec{k}	Band 1	Band 2	Band 3	Band 4
Γ	(0, 0, 0)	≈ 0	$4E_L - V_2$	$\approx 4E_L + V_2$	$\approx 4E_X$
L	$(\frac{1}{2}, \frac{1}{2}, \frac{1}{2})$	$(\frac{7}{3}E_L - V_1) - A$	$(\frac{7}{3}E_L + V_1) - B$	$(\frac{7}{3}E_L - V_1) + A$	$(\frac{7}{3}E_L + V_1) + B$
X	(1, 0, 0)	$E_X - V_2$	$(\frac{3}{2}E_X + V_2) - C$	$2E_X - V_2$	$(\frac{3}{2}E_X + V_2) + C$
U	$(1, \frac{1}{4}, \frac{1}{4})$	$E_U - V_2$			
W	$(1, \frac{1}{2}, 0)$	$E_W - V_2$	$E_W - V_2$	$E_W + V_2 - 2V_1$	$E_W + V_2 + 2V_1$

^a Eigenvalue entries are given relative to the empty lattice choice of energy zero.

^b According to the notation of L. P. Bouckaert, R. Smoluchowski, and E. Wigner [Phys. Rev. 50, 58 (1936)].

erated from the contents of the bins, after all \vec{k} vectors has been sampled.

The absolute value of the DOS is given in Fig. 4. Similar structure in the range of the Fermi level has also been reported by others.^{11, 33} This departure from an $E^{1/2}$ dependence reflects the departure of the free-electron bands from parabolicity, upon contact with the zone boundaries. The tailing off of the DOS at ~ 19 eV means that the four-band model is running out of electrons.

A bonus of this check on our numerical procedures was that it also gave a measure of the self-consistency of Ashcroft's¹⁰ pseudopotential model far away from the Fermi surface. It should be noted that Ashcroft obtained his Fermi level by adjusting the highest energy level of occupancy until $\frac{3}{2}$ the volume of the Brillouin zone was filled. Since the fcc conventional cell of Al had four atoms, each contributing three electrons to these valence bands, we found the electron density

$$\rho = N/V = 12/a^3 = 1.818 \times 10^{23} \text{ electrons/cm}^3, \quad (14)$$

with $a = 4.04145 \text{ \AA}$, as a basis with which to compare the results for electron concentration

$$\rho(E_F) = \frac{N}{V} = \int_0^{E_F} D(E) dE \quad (15)$$

for successive values of E_F . We obtained the results given in Table III. This table gives a Fermi level, by comparison with Eq. (13), of 11.7 eV. Now Ashcroft obtained the value 11.647 eV. When we recall that our energy bins E_m were of width 0.1 eV, we find the agreement admirable. This calculation provides further confirmation of the utility of this pseudopotential, away from the Fermi level.

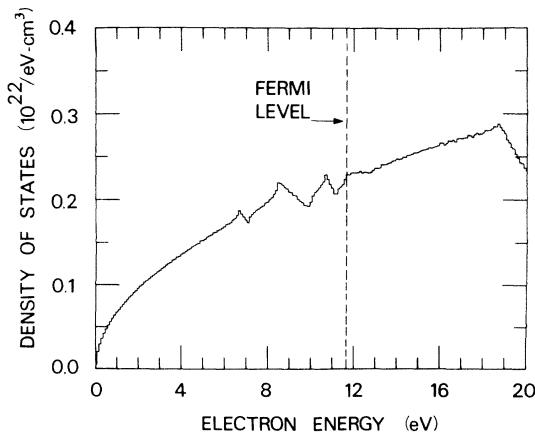


FIG. 4. Electron density of states (DOS) for Al in absolute units.

D. Interband contribution to ϵ_2

The next stage of our computation was the generation of the interband contribution to ϵ_2 . This was designed to provide the ultimate test of our procedures, since the DOS calculation only involved the eigenvalues. Our choice of energy bin width allowed a ready comparison of this four-band model with the nine-band model of Brust,¹¹ who used a similar energy step.

The interband contribution to ϵ_2 is given by the standard result³⁴ for isotropic crystals

$$\epsilon_2(E) = \frac{4\pi^2 e^2 \hbar^2}{3m^2 E^2} \frac{2}{(2\pi)^3} \times \sum_{i,f} \int_{\text{BZ}} d^3k |M_{if}(\vec{k})|^2 \delta [E_f(\vec{k}) - E_i(\vec{k}) - E], \quad (16)$$

where $E = \hbar\omega$ and all similar terms have the same meaning as in the definition of the JDOS for absorption in Eq. (2). The essentially new term is $|M_{if}(\vec{k})|^2 = |(U_{\vec{k},f} | \nabla | U_{\vec{k},i})|^2$, where $U_{\vec{k},f}$ and $U_{\vec{k},i}$ represent the Bloch functions. These Bloch functions are obtained by factoring Eq. (9) in the form $\phi_{\vec{k}}(\vec{r}) \equiv U_{\vec{k}}(\vec{r}) e^{i\vec{k}\cdot\vec{r}}$ so that immediately

$$U_{\vec{k}}(\vec{r}) = a_{\vec{k}} + a_{\vec{k}-(1,1,1)} e^{-i(1,1,1)\cdot\vec{r}} + a_{\vec{k}-(1,1,\bar{1})} e^{-i(1,1,\bar{1})\cdot\vec{r}} + a_{\vec{k}-(2,0,0)} e^{-i(2,0,0)\cdot\vec{r}}. \quad (17)$$

Note that Eq. (16) is in fact the JDOS if we ignore the terms $|M_{if}(\vec{k})|^2$ and $4\pi^2 e^2 \hbar^2 / 3m^2 E^2$. In many semiconductors, this matrix element can be treated as a constant. It follows that a knowledge of the JDOS accounts for the structure of ϵ_2 . In simple metals, however, this matrix element is a strong function of \vec{k} .

As in Eq. (13), we cast ϵ_2 into a form convenient for calculation.³⁵ This led to

TABLE III. Evaluation of the Fermi level E_F , by trial integration of the DOS to give electron density ρ . From the known lattice constant, we have $\rho = 1.818 \times 10^{23}/\text{cm}^3$ as a base for comparison.

Trial E_F (eV)	$\rho(E_F)$ (10^{23} electrons/cm ³)
11.5	1.7699
11.6	1.7922
11.7	1.8151
11.8	1.8380
11.9	1.8612

$$\epsilon_2(E_m) = \frac{1}{3} \frac{e^2 \hbar^2}{\pi m^2 E_m^2} \frac{(\Delta k)^3}{\Delta E} \sum_{\vec{k}}' L V_{\vec{k}} \sum_{i,f} |M_{if}(\vec{k})|^2 \Delta \left(E_m - \frac{\Delta E}{2}, E_f(\vec{k}) - E_i(\vec{k}), E_m + \frac{\Delta E}{2} \right), \quad (18)$$

with

$$\Delta \left(E_m - \frac{\Delta E}{2}, E_f - E_i, E_m + \frac{\Delta E}{2} \right) = \begin{cases} 0, & |E_f - E_i - E_m| > \frac{\Delta E}{2}, \\ 1, & |E_f - E_i - E_m| \leq \frac{\Delta E}{2}. \end{cases}$$

The procedure for constructing the histogram of ϵ_2 followed the steps taken in constructing the DOS, with the following exceptions: the addition of the momentum matrix element, the double sum over band indices, and the primed sum over \vec{k} (as before, the prime denoted $E_f > E_F \geq E_i$). The results for ϵ_2 are presented in Fig. 5. For comparison, Brust's nine-band model results are plotted on the same scale. The agreement at the 0.5-eV structure is fair. Presumably the source of the disagreement is due to "convergence" errors. At several symmetry points Brust used a 125-band model to evaluate more accurate bands than the nine-band results. The four- and nine-band results did not "converge" to these best bands, and the differences between the four- and nine-band results were sometimes ~ 0.2 eV.

By contrast, the agreement at the 1.5 eV structure is excellent. Apparently the convergence errors represent a lesser relative part of the energy differences at the higher-photon energy range. The comparison of this type of calculation with ϵ_2 spectra generated from reflectance measurements has been carried out at length.^{11, 35-38} Suffice it to say here that these results accounted for the experimental ϵ_2 spectra nicely.

Two features were of immediate interest. First, we could proceed with a very similar calculation for the spontaneous recombination rate in Al, with confidence that our band structure (eigenvalues and eigenfunctions) was properly assembled. Second, the parallel-band model and these full calculations assure interband structure at $\sim 2V_{111}$ (0.5 eV) and $\sim 2V_{200}$ (1.5 eV) for photon absorption. The proposition we confronted was whether or not this full (full meaning matrix elements included) calculation for photon emission would lead to structure other than that predicted simply on the basis of parallel bands (the parallel-band model is based on JDOS argument, which is never entirely satisfactory in the case of metals).

E. Spontaneous recombination rate-model I

The direct recombination we envisaged, involved an electron making a downward vertical transition from a band below the Fermi level to a hole, gen-

erated by ion impact further down. Here we did not consider the recombination due to excited electrons falling from states above the Fermi level; a second model discussed in Sec. V F involves an excited band.

We rewrote the primed integral for the JDOS for emission, Eq. (5), in the form

$$J(E) = \frac{2}{(2\pi)^3} \sum_{i,f} \int_{\text{BZ}} d^3k \mathcal{F}_i (1 - \mathcal{F}_f) \times \delta[E_i(\vec{k}) - E_f(\vec{k}) - E], \quad (19)$$

where at thermal equilibrium \mathcal{F}_i was the Fermi distribution function, $\mathcal{F}_i = (1 + e^{(E_i - E)/kT})^{-1}$. Under charged-particle bombardment or photoexcitation, this distribution function $\mathcal{F}(E)$ departed from thermal equilibrium and the JDOS obtained a finite value for metals [$J(E)$ vanishes at thermal equilibrium since $1 - \mathcal{F}(E_f) = 0$, when $E_F \geq E_i > E_f$ unless the temperature is exceeding high].

With these notions, we wrote the spontaneous electron-hole recombination rate due to direct transitions^{26, 39, 40} as

$$r(E) \propto E \sum_{i,f} \int_{\text{BZ}} d^3k |M_{if}(\vec{k})|^2 \times \mathcal{F}_i (1 - \mathcal{F}_f) \delta[E_i(\vec{k}) - E_f(\vec{k}) - E]. \quad (20)$$

This expression gave the rate at which photons of energy $E = \hbar\omega$ were emitted per unit energy interval $dE = \hbar d\omega$. We let the following distribution function describe the perturbed metal:

$$\mathcal{F}_i = \begin{cases} 0, & E_i > E_F, \\ 1, & E_i \leq E_F, \end{cases} \quad (21)$$

$$\mathcal{F}_f = \sigma, \quad E_f < E_F.$$

This σ was assumed to be a small arbitrary constant. That is, the generated holes were frozen, and the supply of electrons for recombination came entirely from the two conduction bands in Al (bands 2 and 3).

The emission rate was rewritten in a form convenient for computation. This led to

$$r(E_m) \propto E_m \frac{(\Delta k)^3}{\Delta E} \sum_{\vec{k}}' L V_{\vec{k}} \sum_{i,f} |M_{if}(\vec{k})|^2 \Delta \left(E_m - \frac{\Delta E}{2}, E_i(\vec{k}) - E_f(\vec{k}), E_m + \frac{\Delta E}{2} \right), \quad (22)$$

with

$$\Delta \left(E_m - \frac{\Delta E}{2}, E_i - E_f, E_m + \frac{\Delta E}{2} \right) = \begin{cases} 0, & |E_i - E_f - E| > \frac{\Delta E}{2}, \\ 1, & |E_i - E_f - E| \leq \frac{\Delta E}{2}. \end{cases}$$

The histogram for the emission rate was constructed by the procedure established above. This emission rate is given in Fig. 6. Most striking is the similarity to the ϵ_2 histogram of Fig. 5. Again, the strongest structure occurred at $\sim 2V_{111}$ (0.5 eV) and $\sim 2V_{200}$ (1.5 eV). A parallel-band model was relevant to this proposed recombination model. The energy band structure in the Appendix illustrates tracking at nearly parallel bands along XU and XW ($2V_{200} \approx 1.5$ eV). We also found nearly parallel bands along LK and LU ($2V_{111} \approx 0.5$ eV).

The surface integral for the JDOS for emission, Eq. (6), accounted for the large contributions to the emission rate on these X and L zone faces. We focused our attention of the denominator of Eq. (6) and saw that nearly parallel bands made anomalously large contributions to this integral. Thus, the optical properties for emission should be similar to those for absorption, in so far as the photon-energy location of strong structure is concerned. Apart from this symmetry between absorption and emission, we found no other structure of interest. We believed there was no *a priori* reason to preclude the possibility of other structure, since the \vec{k} dependence of the matrix

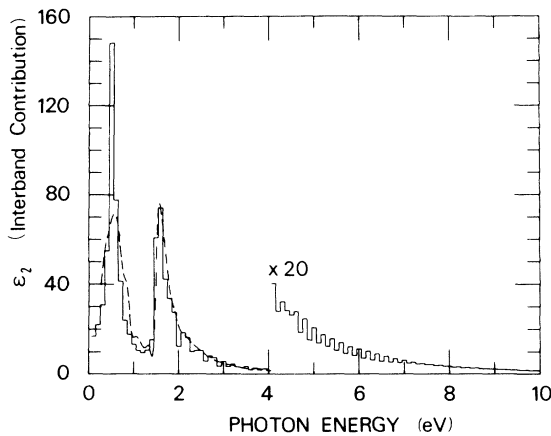


FIG. 5. Interband contribution to the complex part of the dielectric constant ϵ_2 . Histogram, present 4-band results; smooth curve, 9-band model of Brust. (The smooth curve was generated for the sake of illustration. It fits Brust's result exactly at his reported energy steps, which are similar to ours.)

elements was so strong. This symmetry may hold for all simple metals.

We see that within this recombination picture there were two conduction bands which could readily fill generated holes (the fourth band lies above the Fermi level). In Mooradian's picture for the electron-hole recombination in Cu, electrons fell from the upper part of the conduction band to generated holes in d bands vertically below. An idea of the relative weight of the contribution of these two conduction bands in Al to the recombination process can be seen from the Fig. 7. These are our computed intersections of the Fermi surface with the (110) plane and are similar to those generated by Harrison.²⁷ Occupied states are uniformly located between the zone boundaries and the Fermi surface. This geometrical construction of the number of occupied states in these two bands (second and third) agreed with our re-

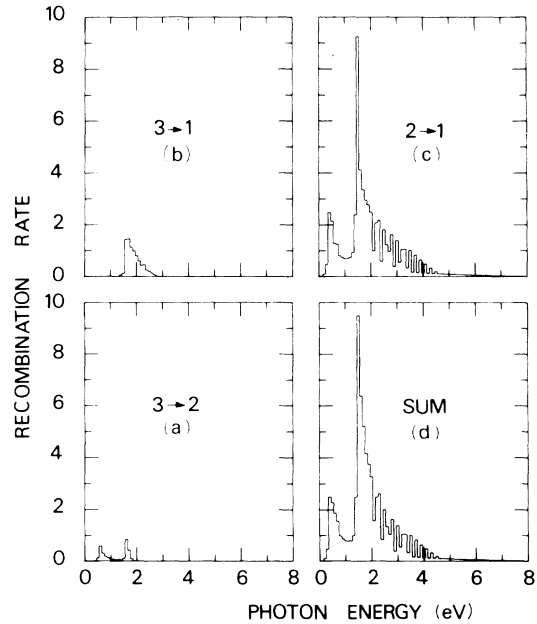


FIG. 6. Computed recombination rate (photons/sec eV, arbitrary units) according to model I. Individual band-pair contributions are illustrated (a) 3→2, (b) 3→1, (c) 2→1. The histogram (d) is the sum of (a), (b), and (c).

sult below that the lower-conduction band (band 2) interacts more strongly with the first band. The contribution to the JDOS of band pairs 2, 1 far exceeds the contributions of band pairs 3, 2 and band pairs 3, 1.

F. Spontaneous recombination rate-model II

We now introduce the second model based on direct interband recombination. This model is similar to the established picture⁹ of luminescence derived from semiconductors and insulators. Inspection of the Al band structure (see the Appendix) shows that there is an excited band (band 4) which has a minimum at a critical point [at a critical point, we have $\nabla_{\mathbf{k}} E_i(\mathbf{k}) = 0$]. This minimum occurs at the W point (there are 24 equivalent W points in the first Brillouin zone). The existence of a minimum in an excited band ensures that a "localized" supply of electrons will be

available, under excitation, to fill vacancies generated below (this is a localization in reciprocal space). Any electron which is excited from band 1, 2, or 3 to band 4 may reach the W point via phonon emission. Further decay can only be radiative, since the minimum at W is energetically isolated from the other bands.

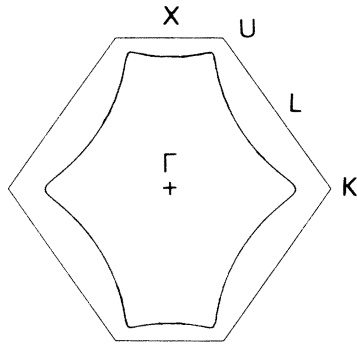
In the spirit of the present calculations, we arbitrarily let the fourth band be occupied up to 0.5 eV above the minimum at the W point. Again we assumed the generated holes were isotropically distributed. The following distribution function described the perturbed metal:

$$\mathcal{F}_i = \begin{cases} 1, & (E_{4,\min} + 0.5 \text{ eV}) \geq E_4 \geq E_{4,\min}, \\ 0, & E_4 > (E_{4,\min} + 0.5 \text{ eV}), \end{cases} \quad (23)$$

$$\mathcal{F}_f = \sigma, \quad E_f \leq E_F.$$

This σ was an arbitrary constant, as above. Only band 4 was used as a source of initial states. $E_{4,\min}$ denoted the band minimum. The emission rate was computed from an expression identical to Eq. (22) except that the Kronecker delta was made consistent with Eq. (23). The resulting histogram is presented in Fig. 8. In the spectral ranges of interest, we have band pairs 4, 2 giving rise to the dominant peak at ~ 1.8 eV, and band pairs 4, 1 giving rise to a weak shoulder at ~ 2.8 eV.

SECOND BAND INTERSECTION



THIRD BAND INTERSECTION

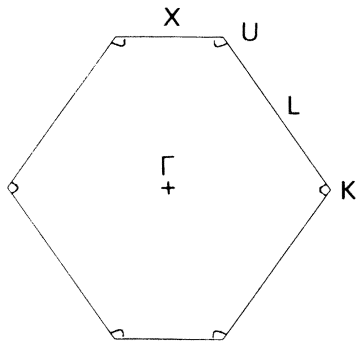


FIG. 7. Intersections of the Al Fermi surface with the (110) plane. (The first band is fully occupied, and the fourth band is empty at thermal equilibrium.) Occupied states lie between the curves and the zone edges. See the Appendix for the band structure.

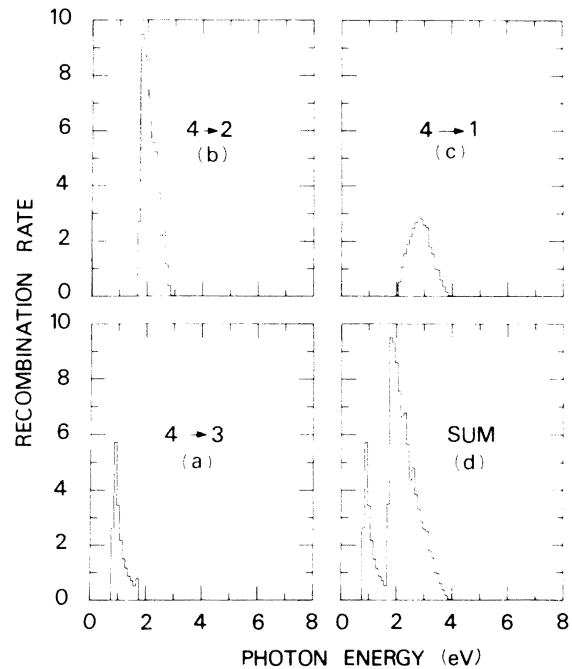


FIG. 8. Computed recombination rate (photons/sec-eV arbitrary units) according to model II. Individual band-pair contributions are illustrated (a) 4 \rightarrow 3, (b) 4 \rightarrow 2, (c) 4 \rightarrow 1. This histogram (d) is the sum of (a), (b), and (c).

VI. COMPARISON OF THEORY AND EXPERIMENT

The results of the two models for the spontaneous recombination rate are quite different (Figs. 6 and 8). Model I predicts an emission spectrum similar to the ϵ_2 spectrum, with structure at 0.5 and 1.5 eV. Model II gives rise to rather different structure at higher energies, 1.8 and 2.8 eV. Both these models are illustrated in Fig. 9, along with the experimental emission for Al. It should be noted that only the experimental data is absolute; both predicted curves are relative and their absolute magnitudes have been fixed to facilitate comparison with experiment.

We regard the degree of correspondence between experiment and model II as encouraging. Our overall objective has been to determine whether the electron-hole radiative recombination process is a plausible explanation of the observed emission. As such, the important question is whether the model predicts emission at the wavelengths where we observe it; clearly the model does this. One of the major inadequacies of the computation is that we have assumed the electron-hole pairs to be uniformly distributed throughout the available bands; this assumption also means that we essentially ignore all details of the collisional excitation process. We could force better agreement between theory and experiment by adopting suitable excitation distribution functions so that the shape of the predicted intensity distribution agrees better with experiment. One cannot expect detailed agreement of theory and experiment until the physics of the collision mechanism is included. The calculation predicts that the maximum of intensity due to recombination of band 4 with 2 should lie at 1.8 eV and the maximum for recombination of band 4 with 1 should lie at 2.8 eV (see Fig. 8). The maximum in the experimentally measured emission occurs at 2.4 (point A in Fig. 9) and there is a weak shoulder at 3.3 eV (point B in Fig. 9); the experimental data thus shows two features but shifted from the predicted energies by about 0.5 eV. The major intensity contributions to the experimentally observed band lie at photon energies where the predicted intensity is also large.

There seems to be little correspondence between the experiment and the calculations by model I. The predicted peak is at 1.5 eV, quite significantly removed from the experimental peak A at 2.3 eV. More important, the observed intensities are most significant at photon energies where the predicted intensities are 5% or less of the maximum. Thus, the first model does not clearly satisfy our basic criterion of predicting the range of photon energies where the greatest intensities are

observed.

We would emphasize that the radiative recombination mechanism can be occurring in only a relatively small proportion of the excitation events. An incoming projectile loses some keV of energy in the first 100 Å or so of target from which radiation can escape; this energy must be lost principally to collisions with electrons. Our observed emission represents only about 0.02 photons per incident ion, with an average photon energy of 2.4 eV. Thus, the energy emitted as radiation represents only one part in 10^5 of the energy lost by the projectile in collisions with electrons. Radiative recombination is a rather rare event.

In conclusion then, we have established that an electron-hole recombination mechanism can plausibly explain the broadband emission when light projectiles strike aluminum. It would appear that the recombination occurs between electrons in the excited band 4 with generated vacancies below. The mechanism is similar to that invoked to explain luminescence in materials other than metals. Close comparison between theory and experiment is probably not warranted until the details of the initial collisional excitation process can be included.

APPENDIX

In performing the calculations discussed in the body of the paper, it was necessary to generate the band structure of aluminum. Previous calculations of band structure generally present graphically, energies along symmetry lines and on zone

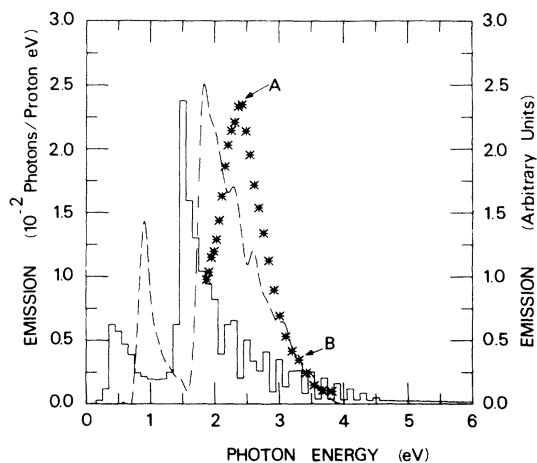


FIG. 9. Theoretical emissive rates according to models I and II (arbitrary units) compared with the absolute value of the experimental emission. Histogram, model I; dashed curve, model II; stars, experimental emission. (For illustration here, the histogram for model II, shown in Fig. 8, has been computer-fit with a dashed curve.)

TABLE IV. The $E_i(\vec{k})$ vs \vec{k} , for band indices $i=1$ through 4, are listed. The first column gives the BSW symbol, where appropriate; the second column specifies \vec{k} (see text); the third column gives the number of like vectors; the fourth through seventh columns gives the energy eigenvalues. Energy is given in electron volts, and the zero of energy is taken to be the bottom of the first band.

Energy band structure of aluminum							Energy band structure of aluminum						
BSW	k	Like k	Band 1	Band 2	Band 3	Band 4	BSW	k	Like k	Band 1	Band 2	Band 3	Band 4
Γ	000	1	0.000	26.880	28.398	36.883	S	811	12	8.751	10.241	14.018	18.866
Δ	100	6	0.141	24.722	26.235	32.431		221	24	1.288	17.304	22.148	28.976
Δ	200	6	0.570	22.851	24.353	28.273		321	48	2.002	15.721	20.560	25.103
Δ	300	6	1.284	21.269	22.726	24.438		421	48	3.002	14.425	19.246	21.533
Δ	400	6	2.285	19.974	20.625	21.654		521	48	4.285	13.415	17.942	18.535
Δ	500	6	3.568	17.428	18.966	20.545		621	48	5.845	12.687	15.171	17.596
								721	48	7.654	12.131	12.640	17.149
Δ	600	6	5.130	14.445	18.247	19.809		821	24	9.183	10.633	12.180	17.002
Δ	700	6	6.940	11.777	17.815	19.372		331	24	2.720	14.140	18.984	25.815
X	800	3	8.463	9.967	17.672	19.226		431	48	3.720	12.845	17.683	22.232
Σ	110	12	0.285	22.563	24.083	32.569		531	48	5.002	11.837	16.657	18.955
	210	24	0.713	20.693	22.207	28.405		631	48	6.561	11.116	15.646	16.251
	310	24	1.428	19.110	20.613	24.537		731	48	8.365	10.678	13.213	15.590
	410	24	2.428	17.815	19.273	20.992		831	16	9.902	10.457	11.478	15.434
	510	24	3.711	16.808	17.465	18.494		441	24	4.725	11.552	16.395	23.232
	610	24	5.272	14.569	16.089	17.671		541	48	6.005	10.546	15.383	19.941
	710	24	7.082	11.912	15.657	17.224		641	48	7.558	9.832	14.645	16.963
Z	810	12	8.607	10.102	15.513	17.077							
Σ	220	12	1.144	18.823	20.343	28.831	Q	741	24	9.214	9.548	13.935	14.574
	320	24	1.858	17.240	18.755	24.957		551	24	7.289	9.548	14.385	21.229
	420	24	2.858	15.945	17.449	21.378		651	24	8.651	9.024	13.662	18.236
	520	24	4.142	14.938	16.396	18.126							
	620	24	5.702	14.219	14.888	15.916	Λ	222	8	1.719	15.495	24.817	29.412
	720	24	7.511	12.321	13.787	15.378		322	24	2.433	13.912	23.218	25.548
								422	24	3.433	12.617	21.668	22.215
Z	820	12	9.039	10.517	13.643	15.223		522	24	4.715	11.609	18.598	20.982
Σ	330	12	2.577	15.657	17.179	25.670		622	24	6.274	10.888	15.616	20.247
	430	24	3.576	14.362	15.880	22.086		722	24	8.079	10.448	12.961	19.811
	530	24	4.859	13.355	14.861	18.800							
	630	24	6.418	12.636	14.095	15.848	U	822	8	9.614	10.208	11.235	19.666
	730	24	8.226	12.204	12.908	13.933		332	24	3.151	12.332	21.652	26.251
Z	830	12	9.758	11.189	12.060	13.688		432	48	4.150	11.037	20.341	22.677
Σ	440	12	4.581	13.068	14.592	23.087		532	48	5.431	10.032	19.080	19.634
	540	24	5.863	12.060	13.582	19.795		632	48	6.984	9.319	16.315	18.682
	640	24	7.420	11.341	12.853	16.808		732	24	8.651	9.024	13.662	18.236
	740	24	9.223	10.909	12.374	14.190		442	24	5.153	9.747	19.063	23.668
								542	48	6.428	8.748	18.040	20.387
W	840	6	10.765	10.765	11.808	12.782							
Σ	550	12	7.152	11.053	12.586	21.084	Q	642	24	7.804	8.211	17.071	17.638
								552	12	7.521	7.942	17.050	21.664
	650	24	8.702	10.334	11.872	18.090							
	750	8	9.902	10.457	11.478	15.434	Λ	333	8	3.869	10.772	24.638	26.984
K	660	4	9.614	10.208	11.235	19.666		433	24	4.866	9.480	23.102	23.636
Λ	111	8	0.429	21.044	25.889	32.714		330	24	2.577	15.657	17.179	25.670
	211	24	0.857	19.173	24.012	28.552		633	12	7.521	7.942	17.050	21.664
	311	24	1.571	17.589	22.411	24.691		443	24	5.862	8.196	22.048	24.401
	411	24	2.571	16.292	20.817	21.404							
	511	24	3.855	15.276	17.741	20.183	Q	543	24	6.951	7.384	20.802	21.343
	611	24	5.416	14.426	14.889	19.447	L	444	4	6.668	7.114	25.114	25.641
	711	24	7.225	12.045	14.169	19.011							

faces. We present here in tabular form (Table IV) a somewhat more complete matrix in the Brillouin zone which should be of value in checking the adequacy of computer programs for generating band structure. To avoid fractions, the wave vectors \vec{k} are given here in units of $\pi/4a$, where a is the lattice constant. These are presented in Ashcroft's¹⁰ choice of $\frac{1}{48}$ symmetry sector. Burdick's⁴¹ discussion details the method of constructing this mesh of 89 \vec{k} values. Since the entire Brillouin zone is not directly sampled in this type of calculation, one can infer the contributions from the entire zone to a calculated property via the number of vectors equivalent by symmetry to those directly used; the algorithm for generating the number of "like vectors" is given by Brust.³²

We also present in Fig. 10, conventional graphical representation of energy bands for various symmetry axes and zone surfaces. The bands are

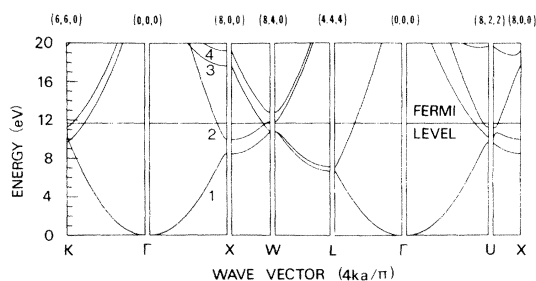


FIG. 10. Energy band structure of Al based on a four-OPW(orthogonalized-plane-wave) model. The results are given within the irreducible sector of the Brillouin zone. Ashcroft's pseudopotential was employed. Bands are indexed 1-4, at fixed wave vector, in order of increasing energy.

presented along more lines, in our results, than elsewhere.¹⁰

*Work supported in part by the NSF.

¹E. S. Parilis, *Atomic Collision Phenomena in Solids* (North-Holland, Amsterdam, 1970), p. 513.

²N. H. Tolk, D. L. Simms, E. B. Foley, and C. W. White, *Radiat. Eff.* **18**, 221 (1973).

³C. Kerkdijk and E. W. Thomas, *Physica (Utr.)* **63**, 577 (1973).

⁴C. B. Kerkdijk, C. M. Smits, D. R. Olander, and F. W. Saris, *Surf. Sci.* **49**, 45 (1975).

⁵W. E. Baird, M. Zivitz, J. Larsen, and E. W. Thomas, *Phys. Rev. A* **10**, 2063 (1975).

⁶W. F. van der Weg and E. Lugujjo, *Atomic Collisions in Solids* (Plenum, New York, 1975), p. 511.

⁷A. Mooradian, *Phys. Rev. Lett.* **22**, 185 (1969).

⁸A. Bonnot, J. M. Debever, and J. Hanns, *Solid State Commun.* **10**, 173 (1972).

⁹See for example Sec. I and IV of *Seventh International Conference on the Physics of Semiconductors, Paris, 1964* (Academic, New York, 1965), Vol. 4.

¹⁰N. W. Ashcroft, *Philos. Mag.* **8**, 2055 (1963).

¹¹D. Brust, *Phys. Rev. B* **2**, 818 (1970).

¹²R. Stair, R. G. Johnston, and E. W. Halbach, *J. Res. Natl. Bur. Stand. (U.S.) A* **64**, 291 (1960).

¹³J. W. McConkey, *J. Opt. Soc. Am.* **59**, 110 (1969).

¹⁴J. F. M. Aarts and F. J. de Heer, *J. Opt. Soc. Am.* **58**, 1666 (1968).

¹⁵E. W. Thomas, G. D. Bent, and J. L. Edwards, *Phys. Rev.* **165**, 32 (1968).

¹⁶D. J. Burns, F. R. Simpson, and J. W. McConkey, *J. Phys. B* **2**, 52 (1969).

¹⁷W. L. Wiese, M. W. Smith, and B. M. Miles, *Atomic Transition Probabilities Volume II*, Natl. Bur. Stand. Rept. No. NSRDS-NBS-22(U.S. GPO, Washington, D. C., 1969), p. 48.

¹⁸G. Dearnaley, J. M. Freeman, R. S. Nelson, and J. Stephen, *Ion Implantation* (Elsevier, New York, 1973), p. 215.

¹⁹C. Kittel, *Introduction to Solid State Physics* (Interscience, New York, 1971), p. 96.

²⁰R. Kelley and C. B. Kerkdijk, *Surf. Sci.* **46**, 537 (1974).

²¹See for example; A. Nouailhat, G. Guillot, and P. Pinard, *J. Lumin.* **5**, 218 (1972).

²²C. W. White and N. H. Tolk, *Phys. Rev. Lett.* **26**, 486 (1971).

²³J. R. Young, *J. Appl. Phys.* **27**, 1 (1956); N. J. Freeman and I. D. Latimer, *Can. J. Phys.* **46**, 467 (1968).

²⁴H. Boersch, C. Radloff, and G. Sauerbrey, *Z. Phys.* **165**, 464 (1961).

²⁵P. Goldsmith and J. V. Jelley, *Philos. Mag.* **4**, 836 (1959).

²⁶A. Mooradian and H. Y. Fan, *Phys. Rev.* **148**, 873 (1966).

²⁷W. A. Harrison, *Solid State Theory* (McGraw-Hill, New York, 1970).

²⁸F. Wooten, *Optical Properties of Solids* (Academic, New York, 1972).

²⁹D. L. Greenaway and G. Harbeke, *Optical Properties and Band Structure of Semiconductors* (Pergamon, Oxford, 1968).

³⁰W. A. Harrison, *Phys. Rev.* **147**, 467 (1966).

³¹R. W. G. Wyckoff, *Crystal Structure* (Interscience, New York, 1951), Vol. I.

³²D. Brust, *Phys. Rev.* **134**, A 1337 (1964).

³³R. Y. Koyama and N. V. Smith, *Phys. Rev. B* **2**, 3049 (1970).

³⁴H. Ehrenreich and M. H. Cohen, *Phys. Rev.* **115**, 786 (1959).

³⁵A. J. Hughes, D. Jones, and A. H. Lettington, *J. Phys. C* **2**, 102 (1969).

³⁶G. Dresselhaus, M. S. Dresselhaus, and D. Beaglehole, *Natl. Bur. Stand. (U.S.) Spec. Pub. No. 323*.

³⁷D. Brust, *Phys. Lett. A* **31**, 289 (1970).

³⁸L. W. Bos and D. W. Lynch, *Phys. Rev. Lett.* **25**, 156 (1970).

³⁹F. Stern, *Solid State Phys.* **15**, 299 (1963).

⁴⁰G. Lasher and F. Stern, *Phys. Rev.* **133**, A 553 (1964).

⁴¹G. A. Burdick, *Phys. Rev.* **129**, 138 (1963).